Sensors & Actuators: B. Chemical 344 (2021) 130180

Contents lists available at ScienceDirect

Sensors and Actuators: B. Chemical

journal homepage: www.elsevier.com/locate/snb

Well-connected ZnO nanoparticle network fabricated by in-situ annealing of ZIF-8 for enhanced sensitivity in gas sensing application

Yong Xia [a,b,d,f], Aifei Pan [a,b,c,d], David W. Gardner [a,b], Sikai Zhao [a,b,e], Adrian K. Davey [a,b], Zhou Li [a,b], Libo Zhao [c,d,f,*], Carlo Carraro [a,b], Roya Maboudian [a,b,**]

[a] Department of Chemical and Biomolecular Engineering, University of California, Berkeley, CA, 94720, USA
[b] Berkeley Sensor & Actuator Center, University of California, Berkeley, CA, 94720, USA
[c] State Key Laboratory for Manufacturing Systems Engineering, Xi'an Jiaotong University, Xi'an, 710054, China
[d] School of Mechanical Engineering, Xi'an Jiaotong University, Xi'an, 710049, China
[e] School of Resources and Civil Engineering, Northeastern University, Shenyang, 110819, China
[f] State Key Laboratory for Manufacturing Systems Engineering, International Joint Laboratory for Micro/Nano Manufacturing and Measurement Technologies, Xi'an Jiaotong University (Yantai) Research Institute for Intelligent Sensing Technology and System, Xi'an, 710054, China

ARTICLE INFO

Keywords:
In-situ annealing
MOFs
Metal oxide nanoparticle network
Gas sensing
AC impedance spectroscopy

ABSTRACT

Low-power microheater platforms are promising in lowering power consumption during gas sensing processes. However, the small amount of activated-material and poor electrical contact greatly affect the sensitivity. Here, via in-situ annealing of a porous metal organic framework (MOF), ZIF-8, using a miniature heater electrode with a fast ramp rate (ca. 60 °C/s), we demonstrate the formation of a well-connected nanoparticle network with high porosity. Nanoparticle networks prepared in-situ exhibit significantly enhanced response to ethanol, defined as the ratio of sensor's resistance before and after gas exposure, compared to ex-situ annealed counterparts (>10 times larger response) and to commercially available nanoparticles (~4 times larger response) at a sensing temperature of 250 °C. The mechanism of the enhanced performance is studied using AC impedance spectroscopy. The results indicate that the large number of highly accessible and effective adsorption sites on the in-situ annealed material are responsible for the enhancement.

1. Introduction

Solid-state gas sensors have attracted great attention in both industrial and research settings due to features of low cost, fast response, good stability, high sensitivity, and ease of integration. Still, they need heating to activate the sensing material, which increases the overall power consumption (>500 mW) and limits battery-powered applications. One attractive approach to address this problem is shrinking the heated area to micrometer scale and thereby reduce power consumption to the mW range for sensing temperature of 500 °C [1,2]. However, the micrometer-sized heating and sensing area also limits the amount of loaded sensing material, which impacts device sensitivity [3]. To compensate for the limited sensitivity of low-power microheater platform, a number of functionalized nanomaterials with high surface area have been developed, such as WS_2-graphene aerogel [4], MoS_2 aerogel [5] and Pt-BN aerogel [6]. Although the aerogels are promising because of the high surface area per device footprint, the process of synthesis is quite complex and time-consuming. Besides, coverage and deposited morphology of the sensing material and material-electrodes contact are hard to control, which additionally hinders further improvements in sensitivity [3].

To address these limitations, in-situ annealed semiconducting metal oxides (SMOX) with sophisticated and large surface area nanostructures are also studied [3,7,8]. Among them, the ordered SMOX nanomaterial templated by polystyrene sphere exhibits promising results because of highly porous structures with good controllability and excellent sensitivity. However, the porous structure is limited by the template and the fabrication scalability is moderate due to relatively complex processes. Another option is using a precursor with a well-defined structure itself as a template, i.e. "self-templating". In this way, the synthesized material can be well-controlled, and the device fabrication can be scaled up by inkjet printing of "precursor ink" followed by in-situ pyrolysis or by a

* Corresponding author at: State Key Laboratory for Manufacturing Systems Engineering, Xi'an Jiaotong University, Xi'an, 710054, China.
** Corresponding author at: Department of Chemical and Biomolecular Engineering, University of California, Berkeley, CA, 94720, USA.
E-mail addresses: libozhao@mail.xjtu.edu.cn (L. Zhao), maboudia@berkeley.edu (R. Maboudian).

https://doi.org/10.1016/j.snb.2021.130180
Received 31 March 2021; Received in revised form 19 May 2021; Accepted 24 May 2021
Available online 28 May 2021

wafer-level annealing process.

In this paper, we report the use of metal organic frameworks as precursors for in-situ synthesis of SMOX since MOFs are a class of porous materials with controllable pores and sizes, and have shown to act as the precursors of SMOX [9]. Here, MOF ZIF-8 is chosen as the precursor, and a well-connected ZnO network is fabricated via fast in-situ annealing of the ZIF-8 precursor on a miniature heater platform. The gas sensing performance is characterized and compared with the ex-situ annealed counterparts, as well as with the commercial ZnO nanoparticles. AC impedance spectroscopy is used to understand the gas sensing behaviors of the in-situ and ex-situ annealed sensors.

2. Experiments

2.1. Chemicals

$Zn(CH_3COO)_2{\cdot}2H_2O$ (analytically pure), 2-methylimidazolate (2-MIM, 99 %), cetyl trimethyl ammonium bromide (CTAB, >98 %), and commercial ZnO nanoparticle (50 nm in size,) were purchased from Sigma Aldrich and used without further purification. Deionized (DI) water was used as solvent for all aqueous solutions.

2.2. Preparation of ZIF-8

The zeolitic imidazolate framework, ZIF-8, was synthesized using a method similar to the one described by Civan et al. [10] 5 mL Zn $(CH_3COO)_2{\cdot}2H_2O$ aqueous solution (60 mg/mL) was cooled in iced water for more than 10 min in advance before usage to reduce its chemical activity. The solution was labeled "A"; 130 μl CTAB aqueous solution (4 mg/mL) was added to 5 mL 2-MIM aqueous solution (240 mg/mL) and sonicated for 10 min to make a uniform dispersion. The solution was labeled "B". Afterwards, solution "B" was put into iced water and stirred (1000 rpm) for 5 min. Then, solution "A" was poured into solution "B" rapidly and the stirring in iced water was kept for 10 s before taking the solution out and settling it down at room temperature (~20 °C) for 2 h. The transparent solution gradually became white slurry in about 10 s which indicated ZIF-8's nucleation and growth. The solution was then washed with DI water several times via centrifuging and sonicating; and the solvent was replaced by 1-butanol. Finally, a milky ZIF-8 in 1-butanol solution was obtained and ready to use.

2.3. Fabrication of gas sensors

Miniature heater electrodes (Fig. S1(a), Alite, Beijing, PRC) were soldered on a ceramic chip carrier (Fig. S1(b)). 0.5 μl ZIF-8 in 1-butanol solution (ca. 40 mg/mL) was drop-casted on the front side of the miniature heater using a micro-pipette. Then, the heater was powered up to 50 °C using a source-meter (Keithley 2400) to evaporate the solvent. The drop-casting and drying process was repeated 4 times and the gold electrodes were fully covered by the white film of ZIF-8. Then, the heater was powered to 350 °C in 5 s (ca. 60 °C/s) and maintained at 350 °C for 2 h. The sensor was further aged at 250 °C in the lab environment (20 °C, 30~40 % relative humidity) for a day before use. The sensor, following this fabrication process, is denoted as "in-situ annealed sensor".

For comparison, the same ZIF-8 in 1-butanol solution was dried at 50 °C and annealed in air using a tube furnace (Lindberg blue M) at 350 °C for 2 h using the maximum ramp rate (~ 60 °C/min) to mimic the in-situ annealing condition. Sensors fabricated by drop-casting the furnace-annealed material are denoted as "ex-situ annealed sensor". The sensor with commercial ZnO nanoparticles was also fabricated and tested, and is denoted as "commercial ZnO sensor".

2.4. Material characterizations

The morphology of the materials was characterized using field-emission scanning electron microscopy (FESEM, Ultra 55, Zeiss) and high-resolution transmission electron microscopy (HRTEM, JEOL 2100 F). The crystal structures of the synthesized materials were characterized by X-ray diffraction (XRD, Bruker AXS D8 Discover GADDS, λ_{Co} = 0.179 nm). To facilitate comparison to prior literatures, the XRD pattern shown here were transformed into Cu Kα using equation of $2d\sin\theta = n\lambda$. Raman spectroscopy of the materials was performed using a JYHoriba LabRAM spectrometer as described in our previous work. The surface chemical state of the as-prepared material was characterized by X-ray photoelectron spectroscopy (XPS, Thermo Scientific ESCALAB 250Xi, Al Kα= 1486.6 eV, calibration: C 1s = 284.8 eV).

2.5. Gas sensing measurement

The sensor mounted in a ceramic package was placed in a 1 cm^3-volume-size chamber for the gas sensing measurement as described in our previous works [7,8]. The gas delivery system was controlled by a home-made Labview program and mass flow controllers (Bronkhurst) with the controlled flow rate of 300 sccm. The electric signal was measured by a source-meter (Keithley 2602A), which was controlled by an open-source Java-based measurement software (Zephyr). The gases, namely, ethanol (Praxair, 978 ppm in N_2), acetone (Praxair, 409 ppm in N_2), formaldehyde (Praxair, 22.1 ppm in N_2), CO_2 (Airgas, 5.038 % in N_2), NO_2 (Praxair, 21.8 ppm in N_2) and dry air (as a diluent) were used for gas sensing with various concentrations.

2.6. AC impedance spectroscopy measurement

AC impedance spectroscopy was conducted using CHI 660D with two electrodes configuration (CE/RE-WE) in the lab environment (30~40 % relative humidity, 20 °C). The sensor was heated up to 250 °C to reduce the system resistance and the DC bias was set 1 V to mimic the gas sensing measurements. The detailed setup is shown in Fig. S2. The AC magnitude was set as 0.7 V to minimize noise and obtain stable output signal. The testing frequency ranged from 0.01 Hz to 1 MHz. The ethanol exposure was achieved by placing a vial with ethanol in a plastic chamber. The concentration of ethanol was estimated as 8 % based on its vapor pressure.

3. Results and discussion

3.1. Material synthesis, characterization and sensor fabrication

The material synthesis and sensor fabrication process are schematically shown in Fig. 1. The optical images of the fabrication process are shown in Fig. S3. The white material of precursor film turned brown first and finally became light yellow during the high temperature (350 °C) annealing step. After cooling down, the material becomes white again. The yellow color at high temperature is believed to be related to V_o defect of metal oxides [11], which are cured during the cooling process.

Scanning electron micrographs of the as-synthesized ZIF-8 precursor and the in-situ/ex-situ annealed materials are shown in Fig. 2. The ZIF-8 particles have uniform size of 156 ± 15 nm and show hexagonal shape (Fig. 2 (a, b)). The as-prepared in-situ annealed material in Fig. 2 (c, d) shows highly porous and well-connected features. The particles are 10's nanometer in width, and are connected to each other to form a porous network. Compared with the in-situ annealed material, the ex-situ annealed material shows much denser structure with 10's of nm-sized particles randomly distributed, as shown in Fig. 2 (e, f).

The obvious structural differences between the in-situ and the ex-situ annealed materials are attributed to the differences of thermal gradients during the annealing process, as shown in Fig. S4. The thermal gradient in the vertical direction is very large in the case of in-situ annealed process since it was annealed from the bottom using the miniature heater (Fig. S4 (a)). During in-situ annealing process, the hot substrate quickly burns the organic linker (2-MIM), and metal oxide (ZnO) backbone forms and grows "vertically" towards the top as the heat

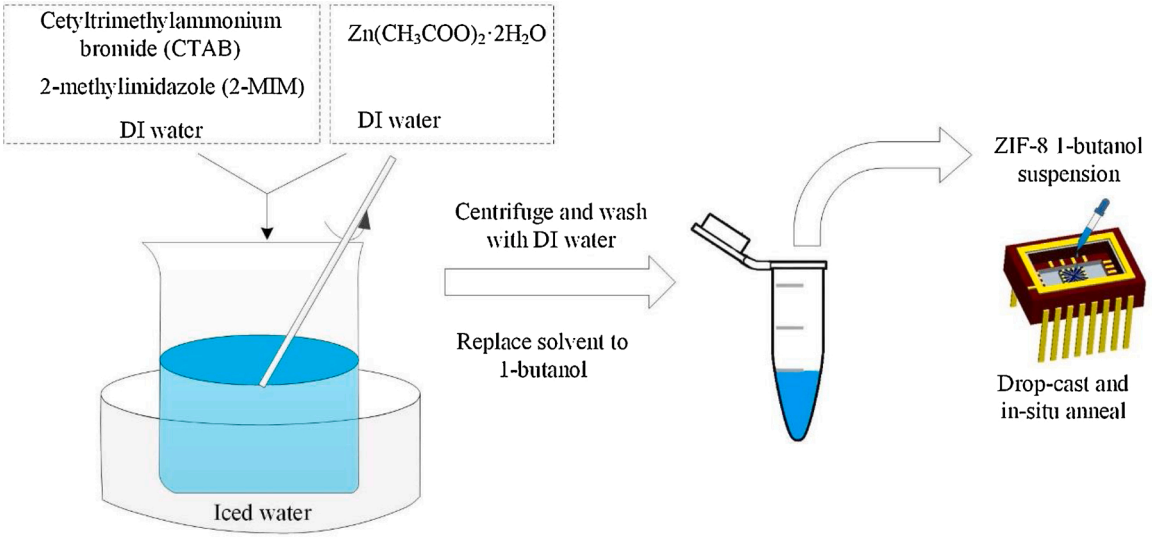

Fig. 1. Schematic view of material synthesis and sensor fabrication.

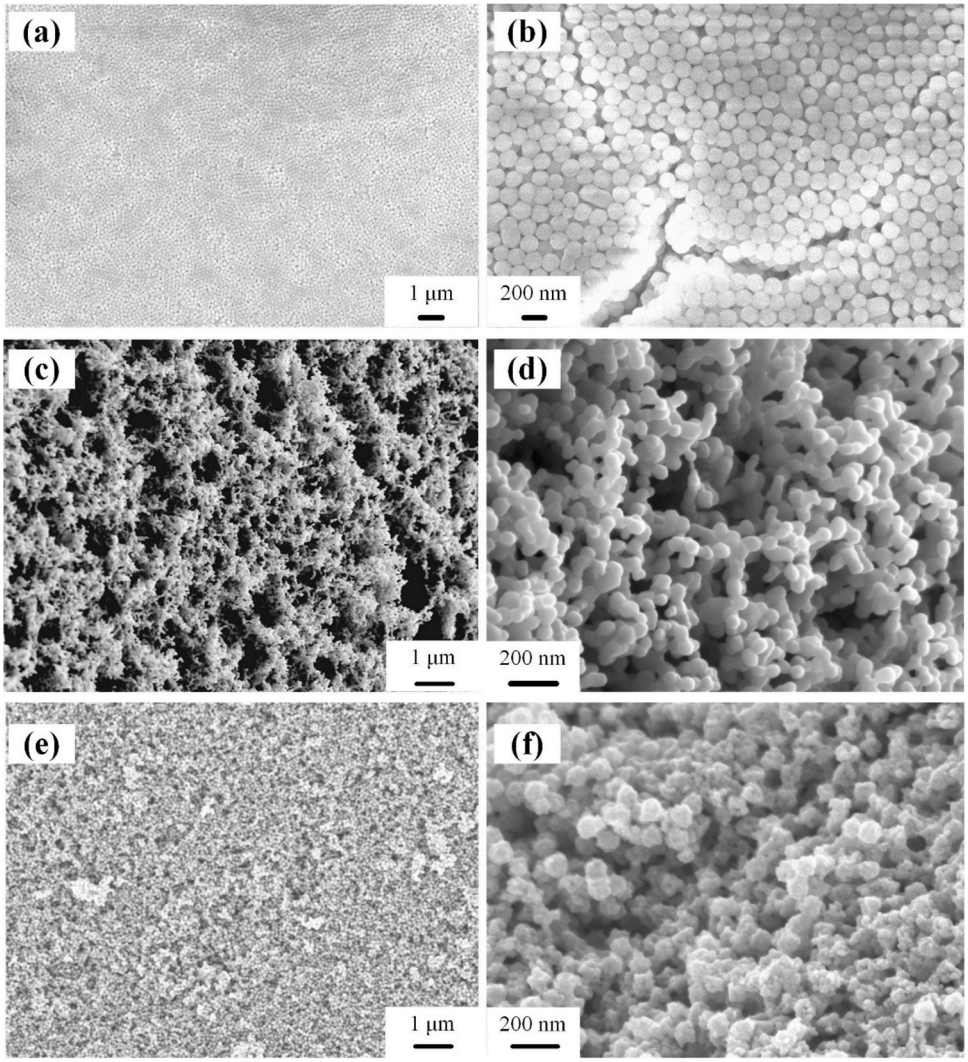

Fig. 2. SEM images of the as-synthesized materials: (a, b) ZIF-8. The low electric and thermal conductivity lead to cracks when taking high-magnification images which is shown in (b); (c, d) in-situ annealed material and (e, f) ex-situ annealed material.

conducts from the bottom to the top layer. Thus, a fractally connected metal oxide network forms. Similar fractal structure is also found in spray pyrolysis synthesized materials [12] where the process has a similar vertical thermal gradient. In contrast, for the ex-situ annealed material, due to the uniform temperature profile in the furnace as shown in Fig. S4 (b), the transformation to metal oxide does not yield bridged (interconnected) structures because they are formed almost simultaneously. The typical thickness of the sensing film fabricated by in-situ annealing is characterized and shown in Fig. S5, which is estimated to be about 7.8 μm.

To further understand the connected structure of the in-situ annealed material, TEM was used, and the results are shown in Fig. 3. The Fig. 3 (a) shows the overall structures of the in-situ annealed material are connected solid particles with 10's to 100's nanometer sizes. Additionally, one could imagine pores with various sizes will form among these connected structures in the as-prepared material. Fig. 3 (b–d) are the high-resolution images of a single particle, particle interface, and particle edge, respectively. The single particle exhibits single crystal feature with lattice fringe spacing of 0.248 nm which corresponds to the (101) plane of hexagonal phase of ZnO. The interface image shows two particles tightly connected with each other in the grain boundary region. In addition, the particle edge image shows there is an amorphous region apart from the nanoparticle. We speculate the amorphous material to be the amorphous ZnO formed during in-situ annealing process since there is no clear boundary between the amorphous material and the crystallized particle. Additionally, the fringe spacing of 0.28 nm is found on other side of the material which is corresponding to plane (100) of hexagonal ZnO.

In addition to morphology, XRD, Raman and XPS spectroscopy were used to characterize the crystal structures, and chemical bonding and chemical compositions/ chemical states of the as-prepared materials, respectively. Fig. S6 shows the XRD pattern of the as-prepared ZIF-8. The peaks fit well with the simulated ZIF-8 spectrum using the crystal model from ref. [13]. Fig. 4 (a) shows the XRD patterns of the in-situ and ex-situ annealed materials. Apart from peaks of the gold electrodes and alumina substrate, both the in-situ and ex-situ annealed materials show peaks at 2θ angles of 31.7, 34.4, 36.2, 47.5, 56.6, 62.8, 66.3, 67.9, 69.0, and 72.5° which match well with the wurtzite ZnO card PDF #36-1451. No other major peaks are found which indicate good purity of the ZnO sensing layer. According to the Scherrer equation, the grain size of the in-situ and ex-situ annealed materials are 23.3 nm and 15.8 nm, respectively. The larger estimated grain size of the in-situ annealed material agrees with the observation of particle size in SEM images of Fig. 2.

The Raman spectrum of as-synthesized ZIF-8 shown in Fig. 4 (b) (bottom black line) has peaks at 178, 286, 688, 838, 955, 1024, 1148, and 1180 cm^{-1} which match well with ZIF-8's Raman modes of *ν*(Zn-N), *ν*(Zn-N), imidazole ring puckering, C-H out of plane bend (C4-C5), C-H out of plane bend (C2-H), C-H out of plane bend, *ν*(C5-N) and *ν*(C-N+N-H wag), respectively [14,15]. This result also agrees well with our XRD results in Fig. S6.

As for the post-annealed samples (in-situ annealed: blue line; ex-situ annealed: red line) shown in Fig. 4 (b), there are peaks at 440 and 580 cm^{-1} which correspond to wurtzite-structured ZnO's Raman modes of E_2 (high) and E_1(LO), respectively. [16,17] The E_1(LO) is usually related to donor defects, such as V_o and Zn_i. [18] Apart from these peaks, peaks at 178 and 235 cm^{-1} are also observed. The peak at 178 cm^{-1} matches the *ν*(Zn-N) of ZIF-8 which is believed to be produced by incomplete pyrolysis. The peak at 235 cm^{-1} is probably a kind of defect state of ZnO. The peak at 277 cm^{-1} corresponding to structural defects of ZnO (possibly N doped ZnO) [19,20] is observed in ex-situ annealed materials but not clearly seen in in-situ annealed materials.

The results of surficial chemical compositions and states of the as-prepared materials characterized by XPS are shown in Fig. 5. Fig. 5

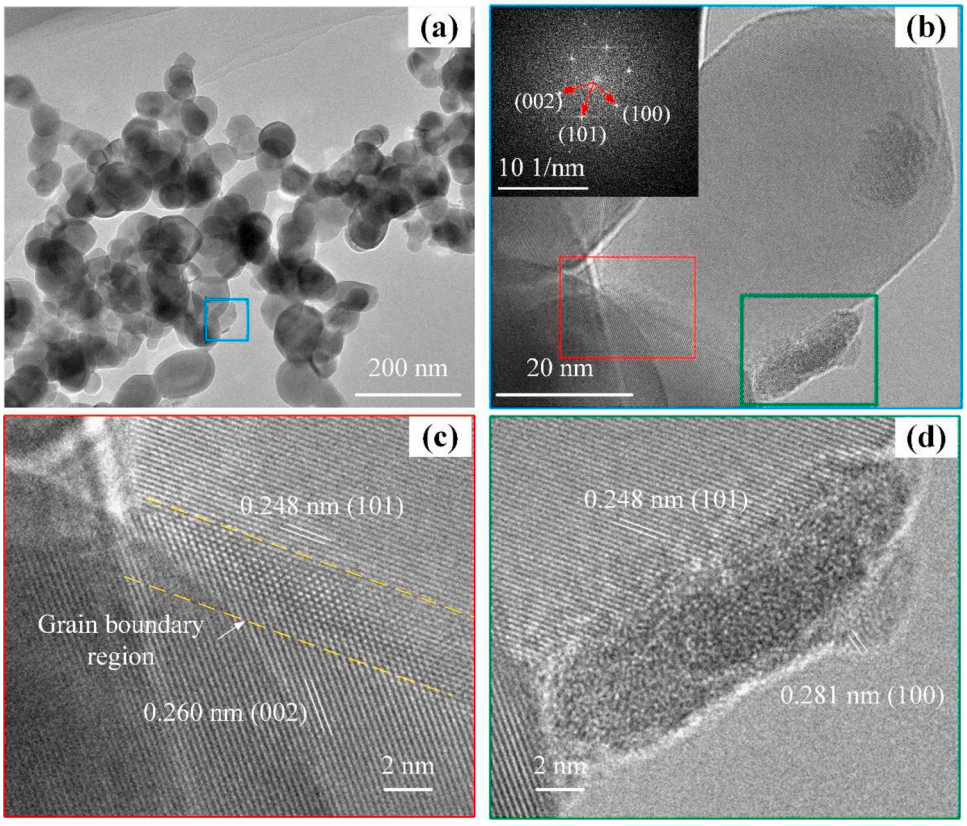

Fig. 3. TEM image of the in-situ annealed material. (a) TEM image; (b) magnified TEM image of a single particle. The inset is calculated electron diffraction map of the particle; (c) high-resolution TEM image at the grain boundary; (d) high-resolution TEM image of the particle edge.

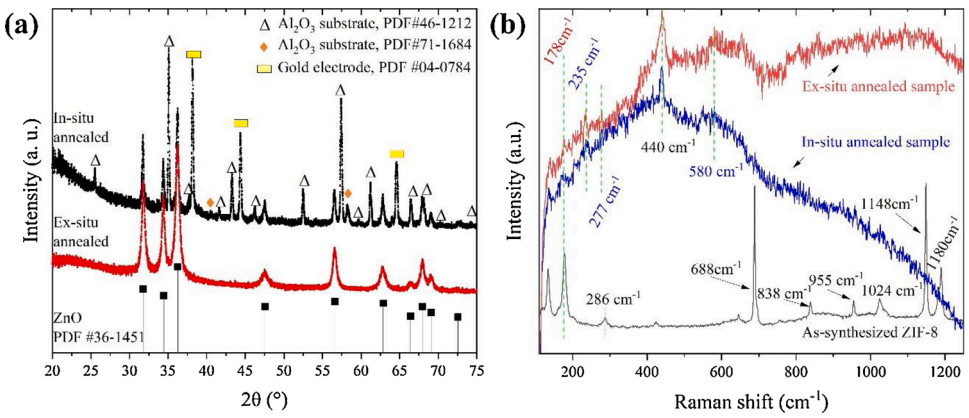

Fig. 4. (a) XRD of the in-situ annealed and ex-situ annealed materials; (b) Raman spectrum of the precursor (ZIF-8) and post-annealed materials (in-situ and ex-situ).

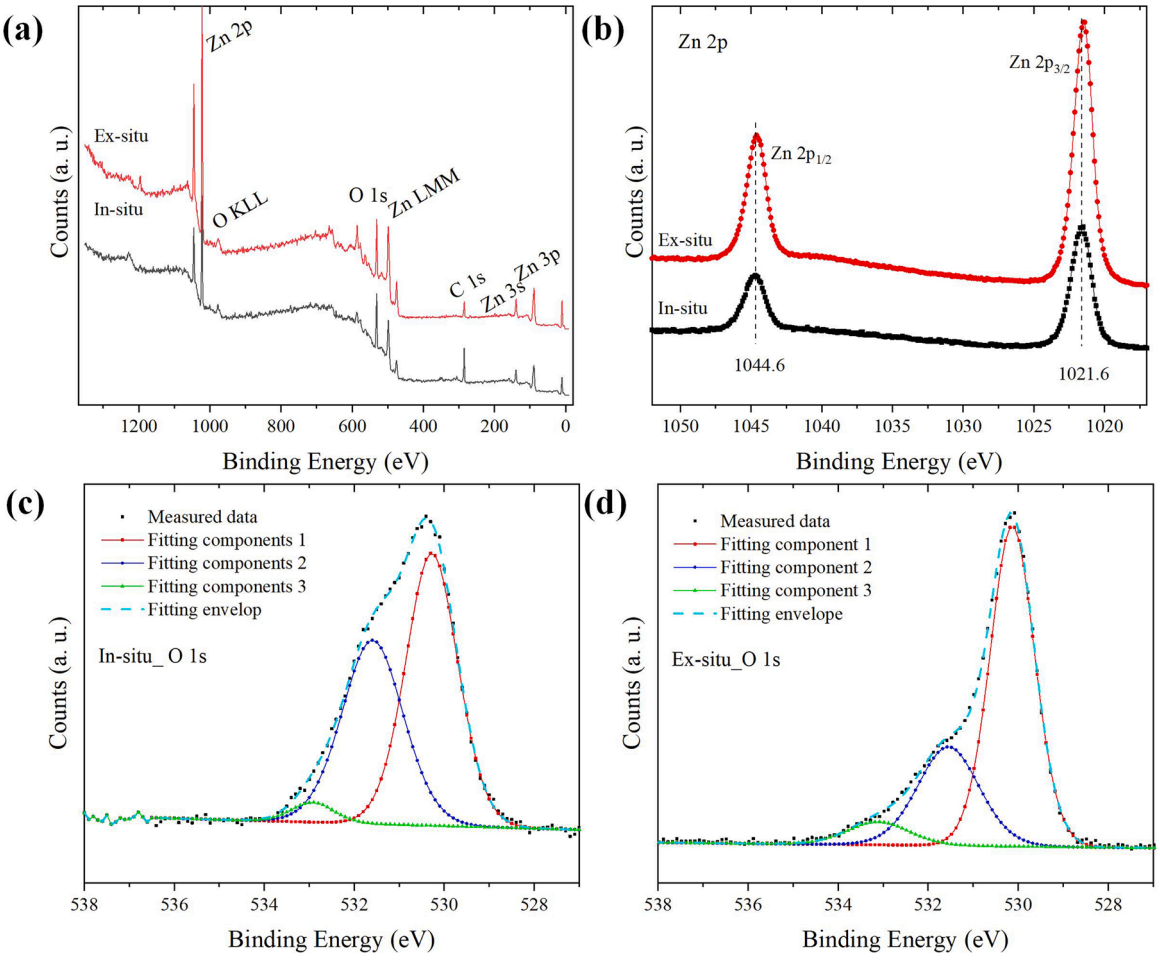

Fig. 5. XPS spectra analysis. (a) Survey; (b) high resolution Zn 2p spectra; (c, d) high resolution O 1s spectra for in-situ and ex-situ annealed material, respectively.

(a) is the survey in which the presence of "Zn", "O" and "C" are confirmed. Fig. 5 (b) is the Zn 2p spectrum where two peaks of Zn $2p_{1/2}$ and Zn $2p_{3/2}$ are observed. The high-resolution O 1s spectrum for in-situ and ex-situ annealed material are shown in Fig. 5 (c) and (d), respectively. Both spectra are asymmetric and can be fitted by 3 peaks with identical full width at half maximum. The peaks at 530.3, 531.6 and 532.9 eV are believed to be lattice oxygen (O_L), lattice oxygen in the oxygen vacancy region (O_v), and chemical adsorbed O_2 and H_2O species (O_{ab}) [11,21]. The analysis shows that the in-situ annealed material exhibits much higher ratio of O_v/O_L, which could be attributed to the ultrafast ramp rate (e.g. ~60 °C/s) induced defects during the fabrication process.

Since there are peaks possibly related to ZIF-8 and N doping in the Raman spectra reported, here, N 1s spectrum was also examined, and the results are shown in Fig. S7. The low signal to noise ratio indicates the concentration of "N" element is relatively low. Still, it can be deconvoluted into several peaks. The peaks at 405.0, 402.4, 399.5 and 398.6 eV could be related to N_2 substitution on oxygen sublattice $(N_2)_O$ in ZnO, [22] pyridine-N-oxide groups, pyrrolic-N, [23,24], and N-Zn-O [25,26], respectively. The broader peaks of in-situ annealed material

indicate the chemical bonds are more complex and less uniform than the ex-situ annealed material. Overall, the nitrogen signal in XPS indicates that both the in-situ and ex-situ annealed materials contain the nitrogen-related functional groups in their near surface regions.

The spectroscopy characterization above confirms the precursor is pure ZIF-8 and both in-situ and ex-situ annealed materials are defect rich, wurtzite structure ZnO. The in-situ annealed material has more complex surface N species and higher relative concentration of O_v than the ex-situ annealed material.

3.2. Gas sensing characteristics

Gas sensing properties of both in-situ and ex-situ annealed devices were evaluated for ethanol, a volatile organic compounds (VOC), since it needs to be monitored, e.g. for drunk driving tests (0 ~ 170 ppm, 0.35 mg/L BrAC, 0.08 % BAC) [27] and a critical exhaled biomarker of fatty liver disease (1~10 ppm) [28]. Ethanol gas sensing tests reported here were performed in the range of 1−10 ppm.

Based on the gas sensing performance, the ramp rate of the in-situ annealed process was optimized to be 60 °C/s as described in part (4) in supplementary materials. The dynamic sensing behavior of in-situ and ex-situ annealed sensors to 10 ppm ethanol at different working temperature is shown in Fig. 6 (a) and (b), respectively. It can be seen that the in-situ annealed sensor has much higher resistance change upon ethanol exposure at different specific working temperatures except for data at 200 °C, where the relative change is similar. The gas response is defined as R_a/R_g, where R_a and R_g are sensor resistance values in air and analytes, respectively. Both the in-situ and ex-situ annealed sensors show much better dynamic response performance in regard to response and response times compared to the commercial ZnO shown in Fig. S9. The response versus working temperature for in-situ and ex-situ annealed sensors is shown in Fig. 6 (c). The in-situ annealed sensor shows a volcano shape at 250 °C where the highest response is achieved. However, the ex-situ annealed sensor shows a decreasing trend with increasing sensing temperature. Combining both the transient plots and the response-working temperature curves, the in-situ annealed sensor shows more temperature-dependent features, which might be attributed to its structure induced sensing features.

To choose the optimum working temperature, the response (t_{res}) and recovery (t_{rec}) times, defined as the times to reach 90 % of the steady-state response and baseline signals, at different working temperatures are calculated and plotted for the in-situ annealed sensor in Fig. 6 (d). Considering the response/recovery times and the sensor response, the working temperature of 300 °C is chosen as the optimum working temperature for both sensors. Additionally, 250 °C is also used in characterizing the sensitivity of the sensors for better comparison.

Fast response and recovery are important parameters in real applications. Therefore, the gas sensing response and recovery times are evaluated at the optimal working temperature of 300 °C. The transient response curves of in-situ and ex-situ annealed sensors to 10 ppm and 1 ppm are shown in Fig. 7 (a, b) and (c, d), respectively. The response and recovery times versus gas concentration at 300 °C are shown in Fig. 7 (e). The recovery times of both sensors show a positive relation to the concentration of ethanol while the response times of both sensors stay almost the same as ~ 1 s among all the concentration levels. This is attributed to the strong ethanol affinity features of the two sensing

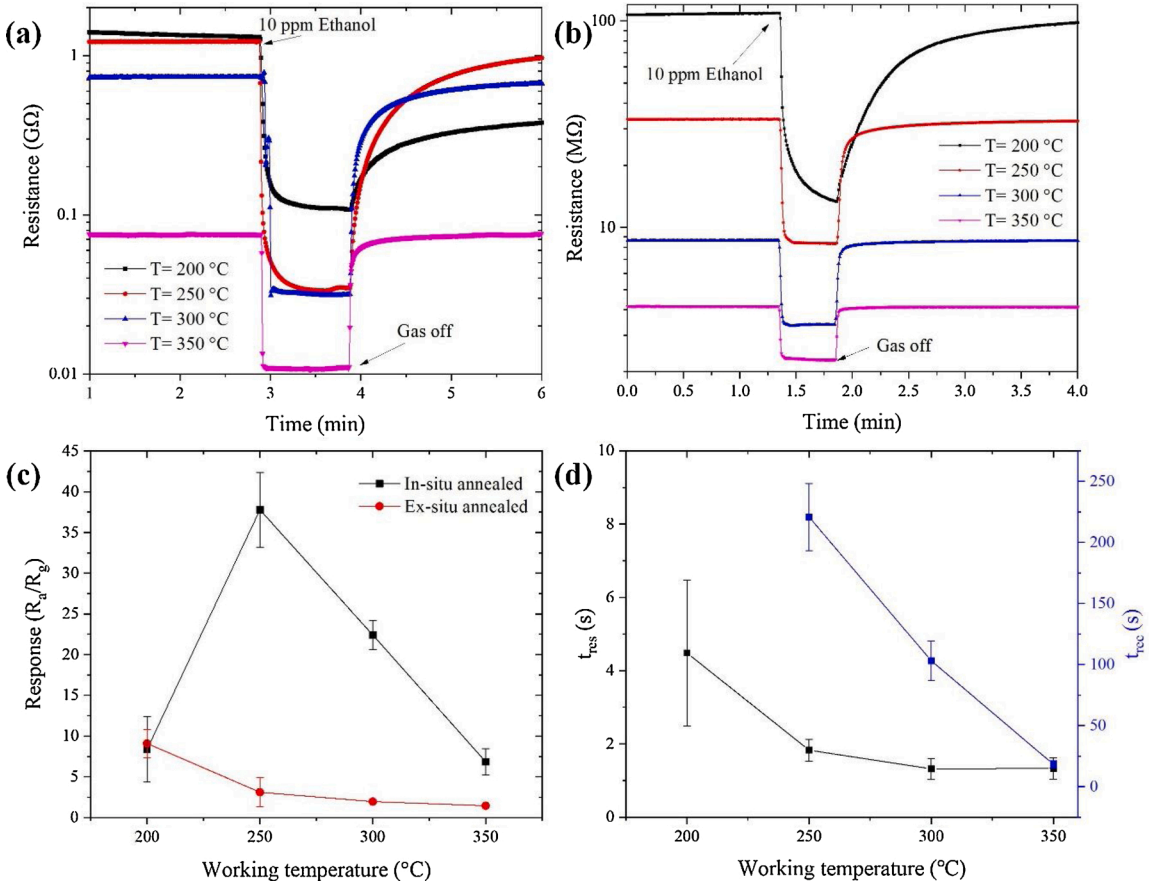

Fig. 6. Optimization of working temperature in response to 10 ppm ethanol. (a) Typical real-time responses of in-situ annealed sensor at different working temperatures. (b) Typical real-time responses of ex-situ annealed sensor at different working temperatures. (c) Sensor response versus working temperatures. (Error bars indicate variations from 3 individual sensors from different batches.) (d) Response/recovery times of in-situ annealed sensor at various working temperature (t_{90} values provided). The recovery at 200 °C is longer than 10 min and not shown here. (Error bars indicates variation from 3 individual test of a senor).

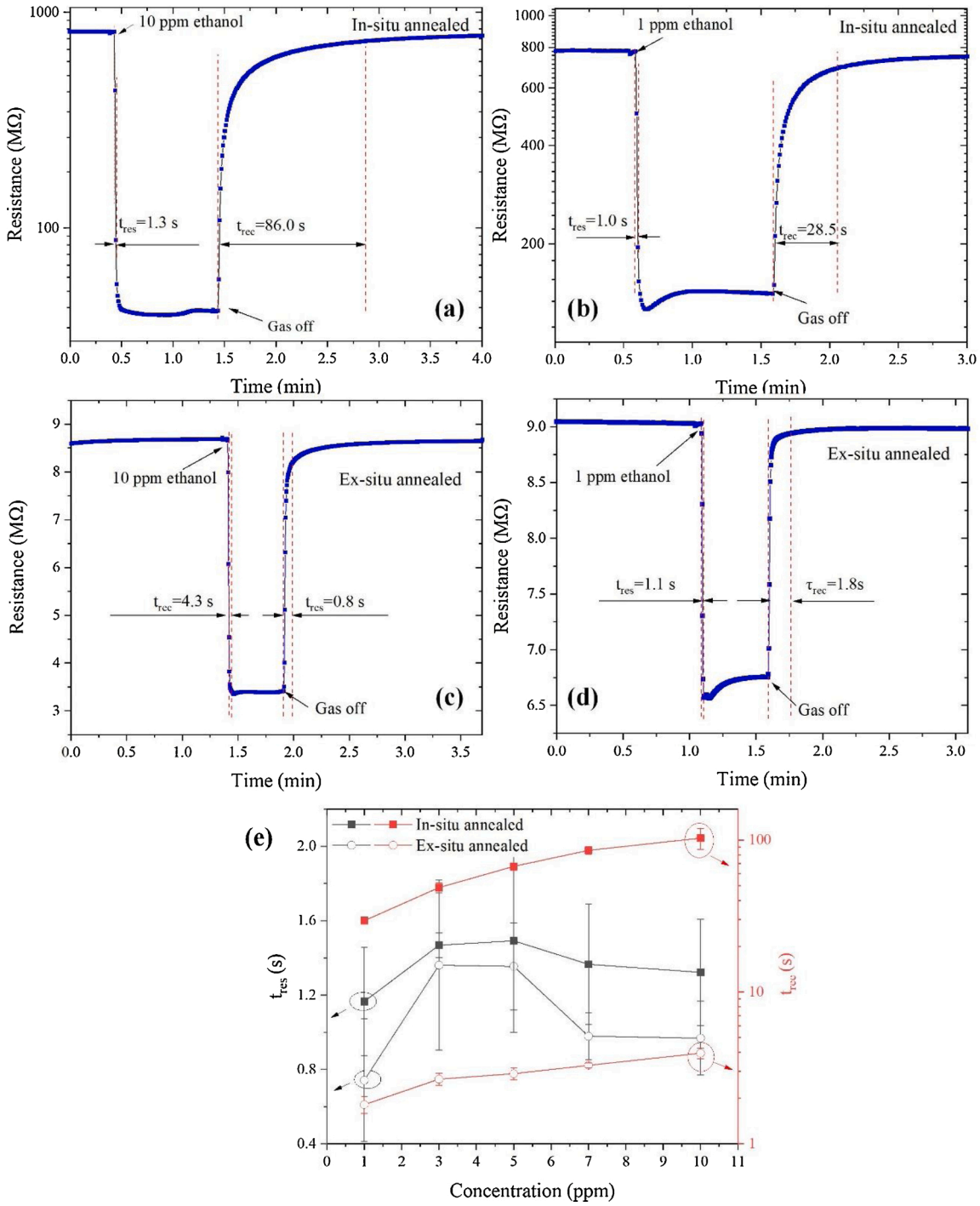

Fig. 7. Response and recovery times of the in-situ and ex-situ annealed sensors to different concentration of ethanol at 300 °C. (a, b) Real-time resistive response of in-situ annealed sensor to 10 and 1 ppm ethanol, respectively. (c, d) Real-time resistive response of ex-situ annealed sensor to 10 and 1 ppm, respectively. (e) Response time and recovery times to different concentration of ethanol. Error bars indicate the variation from 3 individual measurements.

materials. The ex-situ annealed sensor exhibits much faster (~20 times) recovery time compared to the in-situ annealed sensors. This is believed to be caused by higher ethanol penetration of the in-situ annealed material, which will be discussed later.

To study the reproducibility, the sensors were exposed to transient ethanol pulses with concentrations ranging from 1 to 10 ppm. Representative responses are shown in Fig. 8 (a, b) and (c, d), for in-situ and ex-situ annealed sensors, respectively. More reproducibility data are available in Fig. S10. It is clearly seen that both sensors exhibit good dynamic responses and good baseline recovery features, which indicate the sensors have good reproducibility. The responses (R_a/R_g) of in-situ and ex-situ annealed sensors to different concentrations of ethanol are shown in Fig. 8 (e). The response of the sensors to ethanol almost linearly increases with the increase in the ethanol concentration ranging from 1 to 10 ppm at two working temperatures. Additionally, it can be seen that with the increase in ethanol concentration, the response of in-situ annealed sensor increases much more rapidly, which indicates higher sensitivity.

The ethanol sensitivity of the sensors is estimated by fitting the response-ethanol concentration curves as shown in Fig. 8 e and Fig. S11.

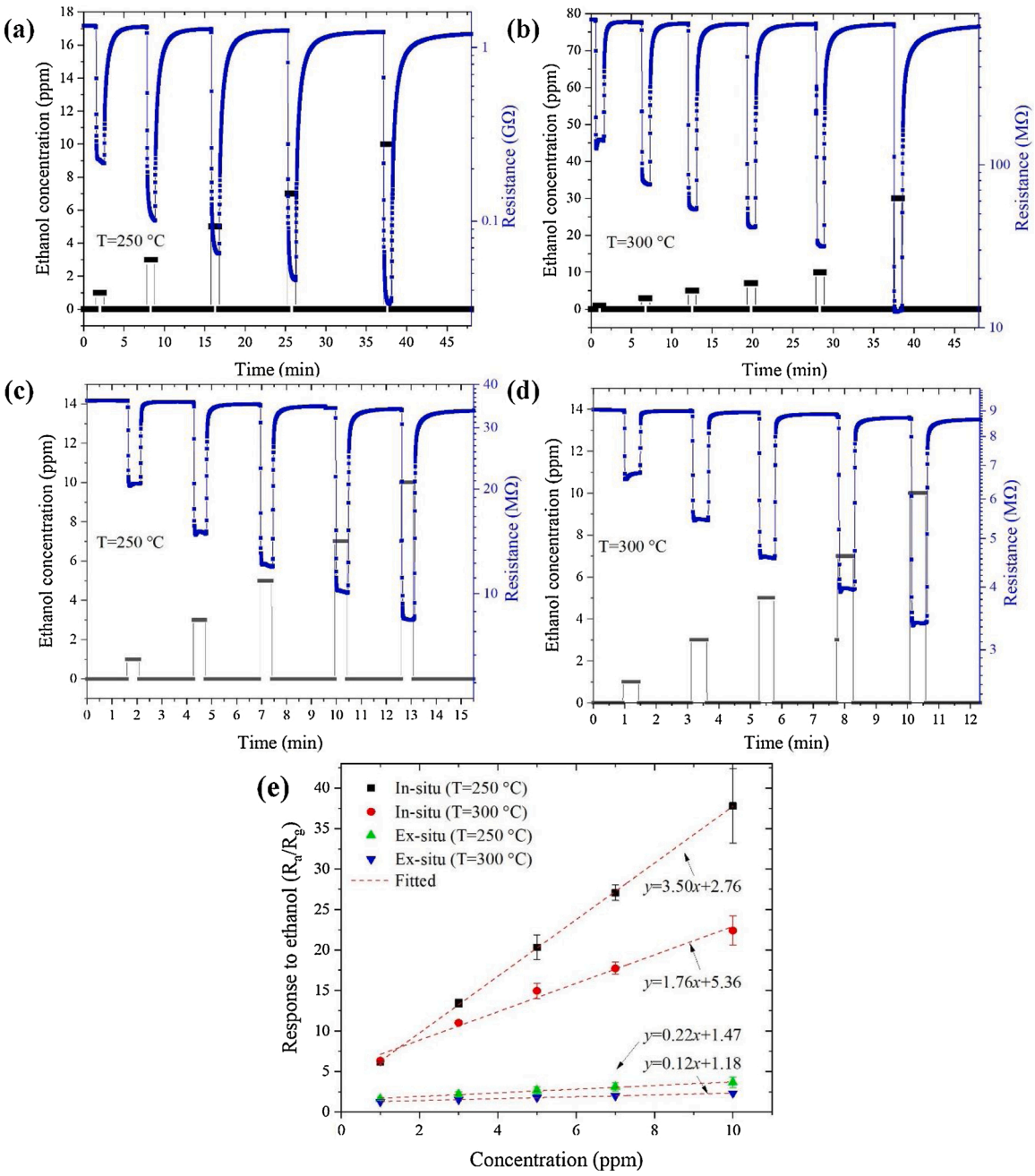

Fig. 8. Gas sensing performance at 250 and 300 °C sensing temperatures. (a, b) Real-time resistive response of the in-situ annealed sensor to increasing concentrations of ethanol. (c, d) Real-time resistive response of the ex-situ annealed sensor to increasing concentrations of ethanol. (e) Sensor response of in-situ and ex-situ annealed sensors versus ethanol concentrations. Error bars are the deviations from 3 individual measurements of a typical device.

The sensitivities of the in-situ annealed sensor, obtained from the slopes, are 3.50 /ppm and 1.76 /ppm at 250 °C and 300 °C, respectively. The sensitivities of the ex-situ annealed sensor are 0.22 /ppm and 0.12 /ppm at 250 °C and 300 °C, respectively. The analysis reconfirms that the in-situ annealed sensor has much higher sensitivity (>10 times) than the ex-situ counterparts at both two working temperatures. The limit of detection (LOD) calculation according to a modified IUPAC method is shown in supplementary material part (8) and Table S1. The LODs are estimated as 1.2 ppb and 1.6 ppb for in-situ annealed sensor working at 250 °C and 300 °C, respectively. Compared to the published ZnO nanomaterials-based ethanol sensors, the developed in-situ annealed sensor exhibited high sensitivity and low detection limit as shown in Table S2.

Another important factor in gas sensing is the selectivity of the sensor. Therefore, the responses of the in-situ and ex-situ annealed sensors are tested at the working temperature of 300 °C to a number of other gases. The selectivity results towards 1 ppm ethanol, 1 ppm acetone, 1 ppm formaldehyde, and 50 ppm CO_2 are shown in Fig. 9. The in-situ annealed sensor shows higher sensitivity to all these gases than the ex-situ annealed sensor but a similar selectivity. All of the sensors showed typical n-type semiconductor behavior of less resistance in the reducing analytes or lower oxygen environment. The mechanism of selectivity is interesting to explore, but it is beyond the scope of this contribution.

Additionally, the long-term stability was also tested and shown in Fig. S14. The result shows that the sensor has a reasonable stability over the first 2 weeks. Future work will focus on understanding the mechanism for limited lifetime and methods to improve it.

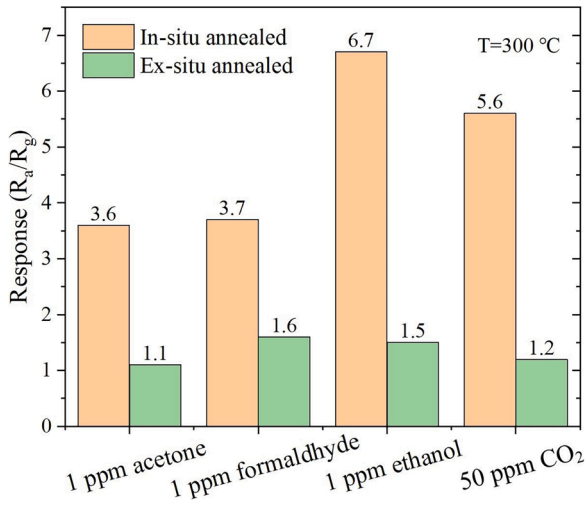

Fig. 9. The responses of the in-situ and ex-situ annealed sensors to select gases at 300 °C.

3.3. Mechanism of the enhanced gas sensing behavior

To understand the enhanced ethanol sensing behavior of the in-situ annealed sensor compared to the ex-situ annealed sensor, AC impedance spectroscopy was employed. The results in air and ethanol are shown in Fig. 10 (a) and (b), respectively. The symbols are the experimental data, while the lines are the fits to the data from corresponding equivalent circuits shown as inset. To minimize the differences and keep a good signal to noise ratio, a working temperature of 250 °C was chosen in this analysis.

Both the in-situ and ex-situ annealed materials have the polycrystalline structure as shown in Fig. 2(d), (f) and 3 (c), where the grain-grain boundary and grain-electrode interface have space charge regions and Schottky barriers, respectively. Therefore, the equivalent circuit of a series resistor (R_1), and two parallel combinations of resistor and capacitor (R_2-CPE_1 and R_3-CPE_2) are used to fit the AC impedance spectra. The series R_1 is usually regarded as resistance of the bulk grain. The parallel combination of a resistor and a capacitor (R-CPE) are used to describe the charge carrier or matter diffusion at grain-grain boundary interface and grain-electrodes interface [29].

The constant phase element, CPE is an idealized circuit element with constant phase angle invariant of frequency. The impedance expression is shown in Eq. (2), where *CPE_T* and *CPE_P* are the constant (or "pre-factor") and diffusion (or "exponent") effect index, respectively [30]. When *CPE_P* equals "1″, "0″, "-1″, and "0.5″, the element equals pure capacitor, pure resistance, pure inductance, and Warburg impedance, respectively [31,32].

$$Z_{CPE} = \frac{1}{CPE\_T \times (j\omega)^{CPE\_P}} \quad (2)$$

The fitting results are tabulated and shown in Table 1.

3.3.1. Grain bulk resistance

The grain bulk resistance (R_1) of the in-situ annealed sensor is smaller than the ex-situ annealed sensor, which could be attributed to the well-connected feature and bigger grain size of the in-situ annealed material. Furthermore, the R_1 increase in ethanol might be related to the intermediate species formed on the grains, which will be explained in the following discussion.

3.3.2. Grain-grain boundary interface

As discussed above, the parallel elements of CPE-R are used to describe interface states of grain-grain or grain-electrodes. However, which one is responsible for grain-grain boundary interface still needs to be determined.

It is reasonable that "R_2", "CPE_1_T", and "R_3" decrease greatly upon exposure to ethanol since ethanol reacts with pre-adsorbed oxygen species (O^- or O^{2-}) and releases electrons back to conduction band. As a result, the space charge layer and grain-grain and grain-electrode barriers become smaller, resulting in decreased resistance and capacitance values [33].

However, it is noticeable that "CPE_2_T" values of both the in-situ and ex-situ annealed sensors increase most significantly among all parameters when exposed to ethanol (10^5 times/ 10^8 times change for in-situ/ ex-situ annealed). We speculate there exists some intermediate products (possibly amorphous carbon) during the extended ethanol exposure. It is probably the intermediate product formed on the grain-grain boundary which greatly increases the capacitance of the grain-grain boundary. Furthermore, the temperature of the material close to the electrodes is much higher than its temperature at the surface grains of the material which allows less intermediate matter to deposit. Therefore, we assign the parallel combination of R_3 and CPE_2 as the contribution of grain-grain boundary.

It is noted that the ex-situ annealed sensor exhibits even larger changes in CPE_2 (both of CPE_2_T and CPE_2_P) upon exposure to ethanol as shown in Table 1. This can be caused by the "piled-up structure" of the ex-situ annealed material that lets the intermediate product penetrate in the grain-grain boundary more easily. The CPE_2-P of the ex-situ annealed sensor in ethanol shifts from "1" to around "0.5", which indicates its transition from capacitor feature to Warburg impedance in ethanol. Nevertheless, the change ratio of "R_3" value, i.e. "*Eval*", for the in-situ sensor is bigger than the ex-situ annealed sensor, which is 5.42E4, almost 5 times bigger than the ex-situ annealed sensor.

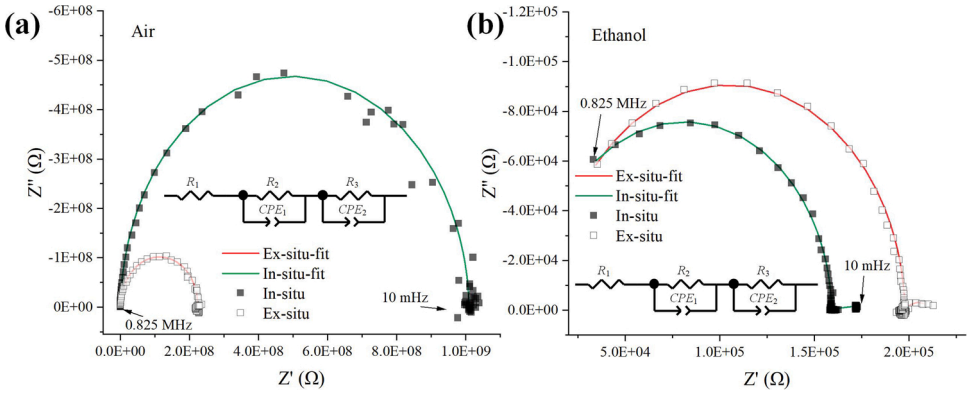

Fig. 10. AC impedance spectroscopy of the ex-situ and in-situ annealed sensors at 250 °C. (a) air background; (b) ethanol background. The insets are the typically used equivalent circuits for polycrystalline materials [22].

Table 1
Fitting values of the components in the corresponding equivalent circuits.

	Parameters						
Sensors	R_1 (Ω)	R_2 (Ω)	CPE_1_T (F)	CPE_1_P	R_3(Ω)	CPE_2_T (F)	CPE_2-P
In-situ (air)	2.62E+03	2.90E+08	7.16E-11	9.80E-01	7.21E+08	1.44E-11	9.80E-01
In-situ (ethanol)	3.62E+03	1.56E+05	3.26E-12	9.84E-01	1.33E+04	2.14E-06	9.23E-01
Eval **	−2.76E-1	**1.86E3***	**2.10E1***	−4.08E-3	**5.42E4***	**−1.00E0***	6.18E-2
Ex-situ (air)	7.68E+03	6.22E+07	1.43E-11	1.07E+00	1.62E+08	4.28E-12	9.71E-01
Ex-situ (ethanol)	1.20E+04	1.86E+05	3.63E-12	9.85E-01	1.41E+04	1.59E-04	5.26E-01
Eval **	−3.60E-1	**3.33E2***	**2.94E0***	8.63E-2	**1.15E4***	**−1.00E0***	**8.46E-1***

* the bolded data are the data with the largest changes.

** *Eval:* $(V_a - V_{ethanol})/V_{ethanol}$, represents the ratio of the change comparing to the value in ethanol since the *response* is calculated as R_a/R_g. The negative values indicate the values in ethanol are bigger.

3.3.3. Grain-electrodes interface

The grain-electrodes interface contribution is thus assigned to the parallel combination of R_2 and CPE_1. It is clearly shown in Table 1 that both R_2 and CPE_1_T values of the in-situ annealed sensor exhibit 6∼7 times higher *Eval* values, which indicate higher degree of electron concentration change upon the ethanol exposure. Combining the multiscale structures of the materials, we ascribe this to the higher porosity and lower gas penetrating resistance of the in-situ annealed material. Furthermore, the values of R_2 and CPE_1_T for the in-situ annealed sensor are larger in air which are attributed to more oxygen adsorption at the grain-electrodes interface inducing thicker space charge layer and higher grain-electrodes barrier. As for the ex-situ annealed sensor, oxygen can hardly reach the grain-electrode boundary and the thus inner part of the material is much more conductive compared to the surface counterparts. As a result, the resistance of ex-situ annealed sensor is controlled by the inner undeleted part. And when exposed to ethanol, the resistance of the ex-situ annealed sensor changed little.

However, the higher gas penetration property could also lead to higher amount of ethanol adsorption/desorption at the grain-electrode interface, which might be responsible for the sluggish recovery observed in the in-situ annealed sensor.

It should also be noted that the changed values of grain-electrodes interface (R_2 and CPE_1) between air and ethanol environment are smaller than the grain-grain boundary (R_3 and CPE_2) for both in-situ and ex-situ sensors. This could be attributed to the relatively higher temperature on the electrodes that prevents the penetration of ethanol molecules.

3.3.4. Overall

The resistance of the in-situ annealed sensor is higher in the air as shown with the values of R_2 and R_3, which agree with the baseline resistances in Fig. 8 (a) and (c). The sensor responses (R_a/R_g) of both the in-situ annealed and ex-situ annealed sensors depend mostly on grain-grain boundary barrier height, followed by grain-electrodes interface barrier, in agreement with the results in the literature [29,34]. The in-situ annealed sensor has much higher response to ethanol than the ex-situ counterparts because the well-connected and porous structure has much higher amount of “accessible and effective materials”.

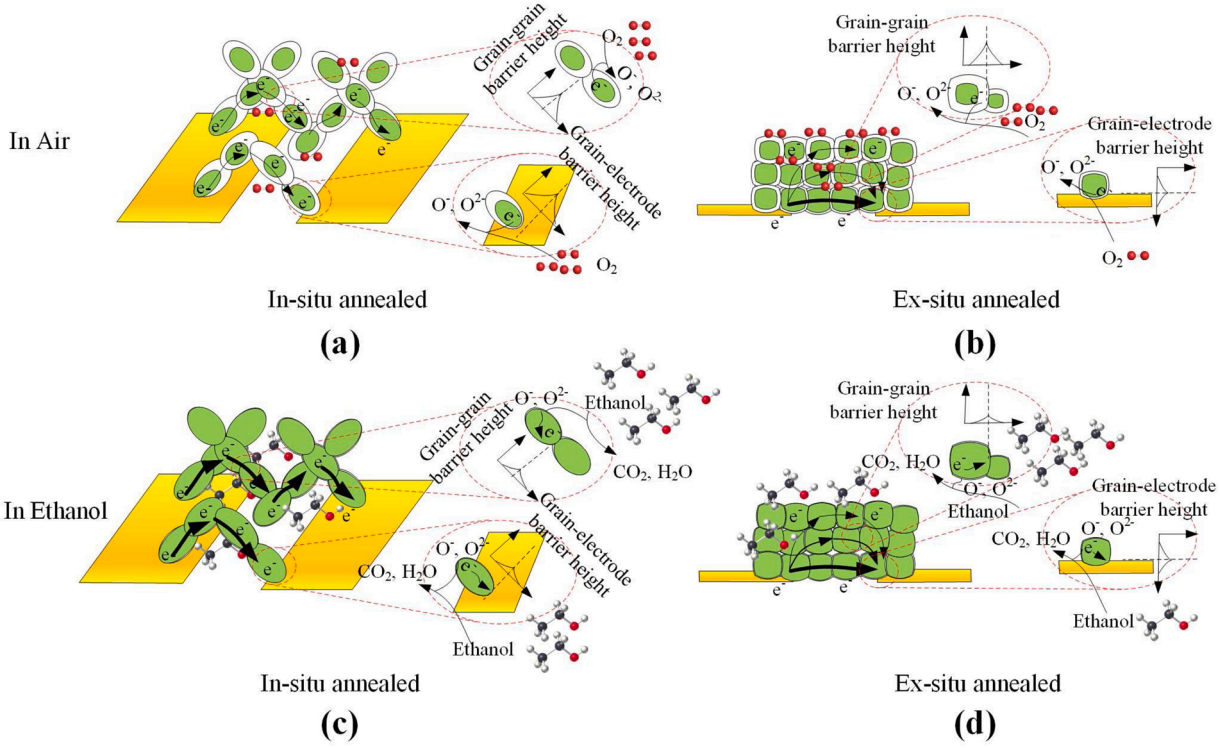

Fig. 11. Schematic view of gas sensing mechanism. The electron depletion layer is shown in white, the unaffected bulk is green, the electrodes are shown in yellow, and thickness of arrows represent current intensity, respectively.

However, it is possibly the structure that allows more gas adsorption/desorption processes to the inner part of the material (e.g. interface of grain-electrode) and limits the recovery speed in the in-situ annealed sensor.

Fig. 11 schematically depicts the proposed sensing mechanisms described by Eqs. (3)–(6) and the different sensing behaviors observed for in-situ and ex-situ annealed sensors. In air, the oxygen adsorbs on the surfaces of the sensing materials, and forms ionized oxygen species, consuming electrons of the sensing material as described by Eqs. (3) and (4). In our cases, following the analysis by Zhang et al. (shown in Fig. S15), the ionized oxygen species in both in-situ and ex-situ annealed sensors at two working temperatures are O^- and O^{2-} [35].

As a result, a thick electron depletion layer forms on the surface of the grains; high grain-grain barrier (back-to-back Schottky barrier [26]) and grain-electrode barrier form as shown in Fig. 11 (a, b) and as evidenced in Table 1:

$$O_2(ads) + 2e^- \rightarrow 2O^-(ads) \quad (3)$$

$$O_2(ads) + 4e^- \rightarrow 2O^{2-}(ads) \quad (4)$$

$$CH_3CH_2OH\ (ads) + 6O^-(ads) \rightarrow 2CO_2\ (ads) + 3H_2O\ (ads) + 6e^- \quad (5)$$

$$CH_3CH_2OH\ (ads) + 6O^{2-}(ads) \rightarrow 2CO_2\ (ads) + 3H_2O\ (ads) + 12e\text{-} \quad (6)$$

In ethanol, the ionized oxygen species are consumed by ethanol as described by Eqs. (5)–(6) and the electrons are released. As a result, the grain-grain and grain-electrodes barriers greatly decrease as shown in Fig. 11 (c, d), and as evidenced by data of ethanol environment in Table 1.

Although the basic sensing mechanism of the in-situ and ex-situ annealed sensors are the same, the in-situ annealed one has higher porosity, lower gas penetrating resistance, and higher amount of "effective sensing material" because of well-connected and porous features. As a result, the degree of change of the grain-electrodes barrier of the in-situ annealed sensor is much higher than the ex-situ annealed sensor, as shown in Table 1. On the other hand, the relative change of grain-grain boundary barrier has less difference since the accessibility is similar. Please note, the similar change in grain barrier height doesn't mean similar resistance change due to different conducting pattern in two kinds of sensors.

For the ex-situ counterparts, the outside layer of the sensing material has a higher resistance due to higher amount of oxygen adsorption inducing thicker depletion layer. But the inner nondepleted layer (smaller resistance) dominates the whole resistance shown with the thicker arrows in Fig. 11 (b) and (d). As a result, the resistance of ex-situ annealed sensor is small, and the response is also small, which is similar to what happens in single nanowire devices with large diameters [33, 36]. In other words, the surface materials are "short-circuited" and become "ineffective".

4. Conclusion

In summary, we have developed a new fabrication method for ZnO material by fast in-situ annealing of MOF ZIF-8, with rich defect features, and well-connected, highly porous structure for gas sensing. The sensitivity towards ethanol is much enhanced (>10 times) while the recovery speed is much smaller (<10 times) compared with the ex-situ counterparts. The mechanism studied by AC impedance spectroscopy and SEM/TEM images indicates the high sensitivity of the in-situ annealed sensor should be attributed to higher gas accessibility of the well-connected porous structure that allows for higher amount effective sensing material and higher amount of reactions at the grain-electrode interface. The sluggish recovery of the in-situ annealed sensor could also be attributed to the larger number of effective gas adsorption sites.

As sensitivity and response/recovery speeds are important metrics in many situations, both the barrier height and material structure should be specifically designed in the future for the next generation of SMOX gas sensors with both high sensitivity and fast response/recovery, since the built-in potential of the barriers can help with charge separation [37], which could boost response and recovery processes.

CRediT authorship contribution statement

Yong Xia: Conceptualization, Investigation, Writing - original draft. **Aifei Pan:** precursor synthesis and writing -review & editing. **David W. Gardner:** writing -review & editing. **Sikai Zhao:** writing – review & editing. Adrian **K. Davey:** writing -review & editing. **Zhou Li:** SEM imaging and writing – review & editing. **Libo Zhao:** Resources, Supervision, Writing - review & editing. **Roya Maboudian:** Conceptualization, Resources, Supervision, Writing - review & editing. **Carlo Carraro:** Writing - review & editing.

Declaration of Competing Interest

The authors declare that they have no known competing financial interests or personal relationships that could have appeared to influence the work reported in this paper.

Acknowledgements

The support of the U.S. National Science Foundation (grant # 1903188) and the industrial members of the Berkeley Sensor & Actuator Center is gratefully acknowledged. The characteration work at the Molecular Foundry is supported by Office of Science, Office of Basic Energy Sciences, of the U.S. Department of Energy under Contract No. DE-AC02-05CH11231. Y.X. acknowledges additional support from the Chinese Scholarship Council. L.Z. acknowledges the National Key Research & Development (R&D) Program of China (grant # 2020YFB2009100), the National Natural Science Foundation of China (grant # 91748207), the Shaanxi Province Natural Science Basic Research Project (2019JC-06), and the 111 Project (grant # B12016).

Appendix A. Supplementary data

Supplementary material related to this article can be found, in the online version, at doi:https://doi.org/10.1016/j.snb.2021.130180.

References

[1] A.C. Harley-Trochimczyk, Environmental Gas Sensing With High Surface Area Nanomaterials on a Low-power Microfabricated Heater Platform, University of California, Berkeley, 2016.
[2] I. Cho, K. Kang, D. Yang, J. Yun, I. Park, Localized liquid-phase synthesis of porous SnO2 nanotubes on MEMS platform for low-power, high performance gas sensors, ACS Appl. Mater. Interfaces 9 (2017) 27111–27119.
[3] A. Rao, H. Long, A. Harley-Trochimczyk, T. Pham, A. Zettl, C. Carraro, et al., In situ localized growth of ordered metal oxide hollow sphere array on microheater platform for sensitive, ultra-fast gas sensing, ACS Appl. Mater. Interfaces (2017).
[4] Wenjun Yan, Marcus Worsley, T. Pham, et al., Effects of ambient humidity and temperature on the NO2 sensing characteristics of WS2/graphene aerogel, Appl. Surf. Sci. (2018).
[5] L. Hu, L. Chan, A. Harley-Trochimczyk, L.E. Luna, R. Maboudian, 3D MoS2 aerogel for ultrasensitive NO2 detection and its tunable sensing behavior, Adv. Mater. Interfaces (2017), 1700217.
[6] A. Harley-Trochimczyk, T. Pham, J. Chang, E. Chen, M.A. Worsley, A. Zettl, et al., Platinum nanoparticle loading of boron nitride aerogel and its use as a novel material for low-power catalytic gas sensing, Adv. Funct. Mater. (2015).
[7] H. Long, S. Turner, A. Yan, H. Xu, A. Zettl, Plasma assisted formation of 3D highly porous nanostructured metal oxide network on microheater platform for low power gas sensing, Sens. Actuators B Chem. 301 (2019), 127067.
[8] H. Long, A. Harley-Trochimczyk, T. He, T. Pham, Z. Tang, T. Shi, et al., In situ localized growth of porous tin oxide films on low power microheater platform for low temperature CO detection, ACS Sens. (2016) acssensors.5b00302.
[9] D. Song, Q.L. Zhu, X. Qiang, Nanomaterials derived from metal–organic frameworks, Nat. Rev. Mater. 3 (2017) 17075.
[10] C. Avci, I. Imaz, A. Carné-Sánchez, J.A. Pariente, D. Maspoch, Self-assembly of polyhedral metal–organic framework particles into three-dimensional ordered superstructures, Nat. Chem. 10 (2018) 78.

[11] J. Wang, Z. Wang, B. Huang, Y. Ma, Y. Liu, X. Qin, et al., Oxygen vacancy induced band-gap narrowing and enhanced visible light photocatalytic activity of ZnO, ACS Appl. Mater. Interfaces 4 (2012) 4024–4030.
[12] Z. Fusco, M. Rahmani, R. Bo, R. Verre, N. Motta, M. Käll, et al., Nanostructured dielectric fractals on resonant plasmonic metasurfaces for selective and sensitive optical sensing of volatile compounds, Adv. Mater. 30 (2018), 1800931.
[13] Crystallography Open Database, Information Card for Entry 4118891, 2021.
[14] D. Radhakrishnan, C. Narayana, Guest dependent Brillouin and Raman scattering studies of zeolitic imidazolate framework-8 (ZIF-8) under external pressure, J. Chem. Phys. 144 (2016), 134704.
[15] G. Kumari, K. Jayaramulu, T.K. Maji, C. Narayana, Temperature induced structural transformations and gas adsorption in the zeolitic imidazolate framework ZIF-8: a Raman study, J. Phys. Chem. A 117 (2013) 11006–11012.
[16] M. Zolfaghari, Propose for Raman mode position for Mn-doped ZnO nanoparticles, Phys. B 555 (2019) 1–8.
[17] M. Ghosh, S. Ghosh, M. Seibt, K.Y. Rao, P. Peretzki, G.M. Rao, Ferroelectric origin in one-dimensional undoped ZnO towards high electromechanical response, CrystEngComm 18 (2016) 622–630.
[18] Z. Wang, J. Xue, D. Han, F. Gu, Controllable defect redistribution of ZnO nanopyramids with exposed {1011} facets for enhanced gas sensing performance, ACS Appl. Mater. Interfaces 7 (2015) 308–317.
[19] M. Ghosh, S. Ghosh, M. Seibt, K.Y. Rao, P. Peretzki, G.M.J.C. Rao, Ferroelectric origin in one-dimensional undoped ZnO towards high electromechanical response, CrystEngComm 18 (2016) 622–630.
[20] C. Bundesmann, N. Ashkenov, M. Schubert, D. Spemann, T. Butz, E. Kaidashev, et al., Raman scattering in ZnO thin films doped with Fe, Sb, Al, Ga, and Li, Appl. Phys. Lett. 83 (2003) 1974–1976.
[21] Z. Geng, X. Kong, W. Chen, H. Su, Y. Liu, F. Cai, et al., Oxygen vacancies in ZnO nanosheets enhance CO2 electrochemical reduction to CO, Angew. Chemie 130 (2018) 6162–6167.
[22] C.L. Perkins, S.-H. Lee, X. Li, S.E. Asher, T.J. Coutts, Identification of nitrogen chemical states in N-doped ZnO via x-ray photoelectron spectroscopy, J. Appl. Phys. 97 (2005), 034907.
[23] L. Zhang, Z. Su, F. Jiang, L. Yang, J. Qian, Y. Zhou, et al., Highly graphitized nitrogen-doped porous carbon nanopolyhedra derived from ZIF-8 nanocrystals as efficient electrocatalysts for oxygen reduction reactions, Nanoscale 6 (2014) 6590–6602.
[24] X. Chen, Z. Zhang, Y. Zhang, B. Yao, B. Li, Q. Gong, Passivation mechanism of nitrogen in ZnO under different oxygen ambience, Crystals 9 (2019) 204.
[25] H. Qin, W. Li, Y. Xia, T. He, Photocatalytic activity of heterostructures based on ZnO and N-Doped ZnO, ACS Appl. Mater. Interfaces 3 (2011) 3152–3156.
[26] O. Game, U. Singh, A.A. Gupta, A. Suryawanshi, A. Banpurkar, S. Ogale, Concurrent synthetic control of dopant (nitrogen) and defect complexes to realize broadband (UV–650 nm) absorption in ZnO nanorods for superior photo-electrochemical performance, J. Mater. Chem. 22 (2012) 17302–17310.
[27] A.W. Jones, The relationship between blood alcohol concentration (BAC) and breath alcohol concentration (BrAC): a review of the evidence, Road Saf. Web Publ. 15 (2010) 1–43.
[28] L. Song, K. Dou, R. Wang, P. Leng, L. Luo, Y. Xi, et al., Sr-doped cubic In2O3/Rhombohedral In2O3 homojunction nanowires for highly sensitive and selective breath ethanol sensing: experiment and DFT simulation studies, ACS Appl. Mater. Interfaces 12 (2019) 1270–1279.
[29] T. Suzuki, A. Sackmann, A. Oprea, U. Weimar, N.J.As. Bârsan, Chemoresistive CO2 gas sensors based on La2O2CO3: sensing mechanism insights provided by operando characterization, ACS Sens. 5 (2020) 2555–2562.
[30] K. Hemalatha, G. Sriprakash, M. Ambika Prasad, R. Damle, K. Rukmani, Temperature dependent dielectric and conductivity studies of polyvinyl alcohol-ZnO nanocomposite films by impedance spectroscopy, J. Appl. Phys. 118 (2015), 154103.
[31] P.B. Srinivasan, J. Liang, C. Blawert, M. Störmer, W. Dietzel, Effect of current density on the microstructure and corrosion behaviour of plasma electrolytic oxidation treated AM50 magnesium alloy, Appl. Surf. Sci. 255 (2009) 4212–4218.
[32] B. Tan, S. Zhang, Y. Qiang, L. Guo, L. Feng, C. Liao, et al., A combined experimental and theoretical study of the inhibition effect of three disulfide-based flavouring agents for copper corrosion in 0.5 M sulfuric acid, J. Colloid Interface Sci. 526 (2018) 268–280.
[33] D. Degler, U. Weimar, N. Barsan, Current understanding of the fundamental mechanisms of doped and loaded semiconducting metal-oxide-Based gas sensing materials, ACS Sens. 4 (2019).
[34] V. Balasubramani, S. Sureshkumar, T.S. Rao, T.J.Ao. Sridhar, Impedance spectroscopy-based reduced graphene oxide-incorporated ZnO composite sensor for H2S investigations, ACS Omega 4 (2019) 9976–9982.
[35] J. Zhang, H. Lu, L. Zhang, D. Leng, Y. Zhang, W. Wang, et al., Metal–organic framework-derived ZnO hollow nanocages functionalized with nanoscale Ag catalysts for enhanced ethanol sensing properties, Sens. Actuators B291 (2019) 458–469.
[36] O. Lupan, L. Chow, T. Pauporté, L.K. Ono, B.R. Cuenya, G.J.S. Chai, et al., Highly sensitive and selective hydrogen single-nanowire nanosensor, Sens. Actuators B: Chem. 173 (2012) 772–780.
[37] R. Chen, F. Fan, T. Dittrich, C. Li, Imaging photogenerated charge carriers on surfaces and interfaces of photocatalysts with surface photovoltage microscopy, Chem. Soc. Rev. 47 (2018) 8238–8262.

Yong Xia is a Ph.D candidate in Xi'an Jiaotong University majoring in Instrument Science and Technology. He received his B. S. degree from Chang'an University in 2013. As a visiting student, he studied synthesis of nanomaterials for gas sensing application in University of California, Berkeley (2018.11–2020.12). His current research interest is micro-nanofabrication for bio-chemical sensors.

Aifei Pan is a Ph.D candidate in Xi'an Jiaotong University majoring in mechanical engineering. As a visiting student in UC Berkeley under the supervision of Prof. Maboudian and Prof. Carraro, she studied MOFs-enhanced SERS based chemical sensing.

David W. Gardner is a Ph. D. candidate in University of California, Berkeley. He received his B. S. from Iowa State University at 2016, majoring in Chemical Engineering. His currently interest is MOFs enabled gas sensors.

Sikai Zhao received his M.S. degree from Northeastern University, China, in 2017 and presently is a Ph.D. student in the School of Resources and Civil Engineering, Northeastern University, China. His current research interests include gas sensors, low-dimensional and composite nanomaterials.

Adrian K. Davey is a Ph.D candidate in UC Berkeley since 2018. He received his B.S. form University of Maryland, Baltimore County (UMBC) majoring Chemical Engineering, in 2018. His current interest is the use of metal-organic frameworks toward colorimetric analyte sensing.

Zhou Li is a Ph.D student of State Key Laboratory of Fire Science, University of Science and Technology of China. His research interest is mainly on metal oxide semiconductor gas sensors. Currently, he works as a visiting graduate researcher under the supervision of Prof. Roya Maboudian in the Department of Chemical and Biomolecular Engineering at University of California, Berkeley.

Libo Zhao was born in Yantai, China, in 1978. He received M.S. degree in Instrument Science and Technology in 2003 and Ph.D. degree in Instrument Science and Technology in 2007, both from Xi'an Jiaotong University, Xi'an, China. He is currently working as a professor in Xi'an Jiaotong University. His research interests include micro and nano-fabrication technology, MEMS sensor technology and precision machining technology.

Carlo Carraro is an adjunct professor in the Department of Chemical and Biomolecular engineering at the University of California, Berkeley. He received his bachelor's degree from the University of Padua, Padua, Italy, and his Ph.D. degree from California Institute of Technology in Pasadena, California. His research interests are in the physics and chemistry of surfaces and synthesis of novel thin-film materials and processes.

Roya Maboudian is a Professor of chemical engineering at the University of California, Berkeley. She received her Ph.D. in applied physics from California Institute of Technology. Her current research interests are in the areas of surface/interfacial science and engineering of micro-/nanosystems, and thin-film science and technology.